

HIGH-PERFORMANCE IMPLEMENTATION OF MATRIX-FREE HIGH-ORDER DISCONTINUOUS GALERKIN METHODS*

STEFFEN MÜTHING[†], MARIAN PIATKOWSKI[†], AND PETER BASTIAN[†]

Abstract. Achieving a substantial part of peak performance on today's and future high-performance computing systems is a major challenge for simulation codes. In this paper we address this question in the context of the numerical solution of partial differential equations with finite element methods, in particular the discontinuous Galerkin method applied to a convection-diffusion-reaction model problem. Assuming tensor product structure of basis functions and quadrature on cuboid meshes in a matrix-free approach a substantial reduction in computational complexity can be achieved for operator application compared to a matrix-based implementation while at the same time enabling SIMD vectorization and the use of fused-multiply-add. Close to 60% of peak performance are obtained for a full operator evaluation on a Xeon Haswell CPU with 16 cores and speedups of several hundred (with respect to matrix-based computation) are achieved for polynomial degree seven. Excellent weak scalability on a single node as well as the roofline model demonstrate that the algorithm is fully compute-bound with a high flop per byte ratio. Excellent scalability is also demonstrated on up to 6144 cores using message passing.

Keywords: High-order discontinuous Galerkin methods · matrix-free methods · sum factorization · SIMD vectorization

1. Introduction. Achieving a substantial part of peak performance on today's and future high-performance computing systems is a major challenge for simulation codes. In this paper we address this question in the context of the numerical solution of partial differential equations (PDEs) with grid-based methods, in particular finite element methods. This field comprises a good part of today's supercomputer applications. As many supercomputers are based on standard components such as multi-core CPUs the techniques discussed in this paper are also relevant on desktop systems.

In the early 2000s the almost effortless increase in performance due to increasing clock rate ended rather abruptly [1]. As a result, the major challenges for simulation software arising from computer architecture today are [19, 32, 20]:

- *Massive Parallelism.* The increase in transistor count per chip has been used to place multiple independent cores (typically 4 to 64) on a CPU chip. Peak performance of such a core is only obtained through the use of SIMD (vector-) instructions where one instruction (such as a fused-multiply-add) is executed on several (say 4 to 16) operands in parallel. In a supercomputer a fixed small number of such CPUs with shared memory are combined in a node and many such nodes are connected via a scalable message passing network. An example of such a system is the 100 Petaflop system TaihuLight [18]. As a consequence, applications on such systems therefore need to harness massive parallelism on the order of 10^6 to 10^9 floating point operations executed simultaneously on three different levels accessible via three different programming models: (i) explicit SIMD instructions, (ii) multiple threads using shared memory and (iii) parallel processes communicating via message passing.
- *Memory gap.* Main (DRAM) memory is not able to deliver operands at

*Submitted to the editors 2017–11–29.

Funding: This project was supported in part by Deutsche Forschungsgemeinschaft under grant Ba 1498/10-2 within the SPPEXA programme. For computational resources the authors acknowledge support by the state of Baden-Württemberg through bwHPC and the German Research Foundation (DFG) through grant INST 35/1134-1 FUGG.

[†]Heidelberg University, Interdisciplinary Center for Scientific Computing, Im Neuenheimer Feld 205, D-69120 Heidelberg, Germany.

{steffen.muething,marian.piatkowski,peter.bastian}@iwr.uni-heidelberg.de

the speed as they are processed in the CPU. This fact has always existed in computer architecture [47] and the introduction of multicore CPUs has brought no relief as the number of memory controllers is typically (much) smaller than the number of cores. Moreover, data transfer from main memory comprises the main energy consumption of a computation. In [32] it was estimated that only 0.1 byte per floating point operation (flop) can be afforded to stay within the power envelope of a future exascale system (about 20 MW). This corresponds to 80 flops to be executed per double precision floating point number loaded from memory. As a consequence it is of great concern to develop algorithms and implementations maximizing the amount of *useful* flops per byte transferred from/to main memory.

- *Heterogeneity.* Many current supercomputing systems employ heterogeneous architectures combining multicore CPUs with one or several coprocessors such as a GPU or the Intel MIC. Coprocessors implement an increased number of simplified cores combined with higher bandwidth to a dedicated memory. Programming such systems requires careful assignment of code parts to CPU and coprocessor and managing the necessary data transfer. Software layers such as OpenACC, OpenCL and Kokkos aim at performance-portable programming of heterogeneous systems which is complicated by the fact that different systems often need different data layout. In this paper we focus on high-performance CPU implementations and do not consider coprocessor architectures explicitly. However, the methodology developed is, in principle, transferable to coprocessor architectures and therefore is also relevant on these architectures.

Finite element (FE) discretization of stationary, nonlinear PDEs (or implicit in time discretization of instationary PDEs) leads to the solution of large and sparse nonlinear algebraic systems of the form $R(z) = 0$. Iterative solution then leads, after linearization (or if the system is linear to begin with), to large sparse linear systems $Az = b$, see e.g. [23, 22]. A basic ingredient of iterative solvers is residual evaluation $r^k = R(z^k)$ and, respectively, operator application $y^k = Az^k$. Note that explicit in time discretization leads to a basic operation of the form $z^{k+1} = z^k + F(z^k)$ where $F(z^k) = M^{-1}R(z^k)$ with M the mass matrix. In particular, when the mass matrix is diagonal this operation can be viewed as a variant of residual evaluation. A single matrix-vector product (with stored matrix A) is memory bound as only two flops are executed per matrix element read from memory (this holds for sparse and dense matrices). Additional complications in the case of sparse matrices such as index access and indirect memory access as well as limited cache reuse on the vectors leads to poor floating point performance (relative to peak performance) of stored matrix vector products even in highly optimized formats [36, 33]. The difficulty of achieving a substantial part of peak performance with implicit, finite-element based PDE solvers is illustrated by the 2015 Gordon Bell prize winner providing the state-of-the-art. The authors of [42] state that their implicit multigrid solver applied to a highly nonlinear earth mantle convection problem is memory bound (despite using a matrix-free high-order discretization) and report in figure 7 an average performance of 7.5 GFlops/s per node which corresponds to 3.5% of peak performance of a BlueGene/Q node (204,5 GFlops/s).

Matrix-free operator application (or residual evaluation and linearized operator application in the nonlinear case) is a promising technique to increase the flop per byte ratio substantially and thus to overcome the memory gap. Obviously, to be faster in real time, this requires to be able to compute matrix entries faster than to

load them from memory. For low order discretizations, this approach is popular with stencil-based codes and constant coefficients [21, 44, 15] but has also been extended successfully to certain types of unstructured meshes e.g. in the HHG software [28]. The situation is fundamentally different for high-order (spectral) finite element methods. Here, the sum-factorization technique for a tensor product basis leads to a *significant reduction of computational complexity* of matrix-free operator evaluation compared to a matrix-vector product [39, 31, 34]. Moreover, the operations can be arranged in a sequence of matrix-matrix products [12] which lend themselves for vectorized execution of fused-multiply-add (fma) instructions. Thus, less operations are executed at a higher rate [34]. Sum-factorization is most easily applied to cuboid elements but has also been used for simplicial elements [31, 43]. It can handle nonlinear problems as well as higher-order geometries and has been used to set up Jacobians [37]. Several established simulation software packages for solving PDEs implement high-order finite element methods using sum factorization, among them nek5000¹, Nektar++², deal.II³ and NGSolve⁴. Here we report on our implementation within the DUNE⁵ software framework [7, 6].

In this paper we combine sum-factorization with discontinuous Galerkin (DG) finite element methods. DG methods are popular in the CFD community due to their local mass conservation property while being higher order convergent (for sufficiently regular problems) and their ability to handle elliptic, parabolic and hyperbolic problems [14]. In particular we are interested in porous media flow applications [24, 30, 5, 35] but the methodology developed here is even more generally applicable. When compared to continuous Galerkin (CG) methods DG involves more degrees of freedom for the same mesh and polynomial degree. This could be alleviated with hybrid DG methods [13] or hybrid high-order methods [41], but we restrict ourselves to the symmetric interior penalty DG method with weighted averages (WSIPG) [26] which performs well for elliptic problems with highly varying, anisotropic diffusion coefficients [4]. A significant advantage of DG methods over CG methods as it turns out is that degrees of freedom can be stored consecutively per element and no gather/scatter operations are necessary to evaluate the element and face integrals. On the other hand, the challenge in DG methods are the interior face integrals where sum-factorization is less efficient due to the lower dimension and the flop per byte ratio is worse. Figure 1 illustrates that computational work for evaluating face integrals is dominating over the work in the volume integrals up to polynomial degree three in $2d$ and five in $3d$. Moreover, more data has to be moved per flop in the face terms.

In addition to operator evaluation, for many problems efficient, robust and scalable preconditioners are essential to achieve fast convergence of iterative methods. While being essential, matrix-free preconditioners are beyond the scope of this paper. We will treat them in a forthcoming paper based on our previous work on low-order subspace correction using algebraic multigrid (AMG) [8]. All operations involving the high-order DG system can be implemented matrix-free while AMG on the low-order subspace provides robustness with respect to anisotropy and high coefficient contrasts. Others have shown good scalability and performance for matrix-free geometric multigrid [28] as well as matrix-free geometric multigrid combined with algebraic multigrid [42]. For this paper we have deliberately chosen to solely concentrate on matrix-free

¹<http://www.mcs.anl.gov/project/nek5000-computational-fluid-dynamics-code>

²<https://www.nektar.info>

³<https://www.dealii.org>

⁴<https://ngsolve.org>

⁵<https://www.dune-project.org>

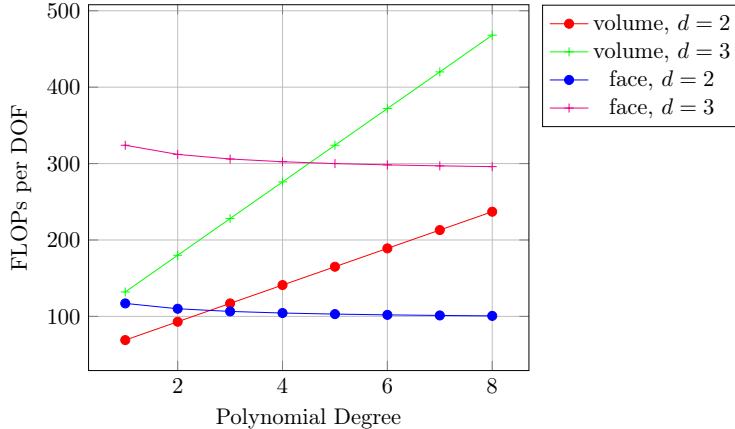


FIG. 1. Number of floating point operations per degree of freedom for sum-factorized volume and face terms in discontinuous Galerkin on a structured mesh in two and three space dimensions.

operator evaluation and matrix-free explicit time-stepping schemes in the context of linear, variable coefficient PDEs.

The rest of the paper is organized as follows: In Section 2 we review the model PDE and its DG discretization, Section 3 describes the sum-factorization technique for discontinuous Galerkin methods while Section 4 provides implementation details before Section 5 presents extensive numerical results and performance evaluation. Then we conclude in Section 6.

2. Continuous Problem and Discontinuous Galerkin Formulation.

2.1. Model Problem. In this work we consider the convection-diffusion-reaction model problem in a finite domain $\Omega \subset \mathbb{R}^d$ and time interval $\Sigma = (t_0, t_0 + T_F]$:

$$\begin{aligned}
 (1a) \quad & \partial_t u + \nabla \cdot (\mathbf{b}u - D\nabla u) + cu = f && \text{in } \Omega \times \Sigma, \\
 (1b) \quad & u = g && \text{on } \Gamma_D \times \Sigma \subseteq \partial\Omega \times \Sigma, \\
 (1c) \quad & (\mathbf{b}u - D\nabla u) \cdot \boldsymbol{\nu} = j && \text{on } \Gamma_N \times \Sigma \subseteq \partial\Omega \times \Sigma, \\
 (1d) \quad & (D\nabla u) \cdot \boldsymbol{\nu} = 0 && \text{on } \Gamma_O \times \Sigma = (\partial\Omega \setminus \Gamma_D \setminus \Gamma_N) \times \Sigma, \\
 (1e) \quad & u = u_0 && \text{at } t = t_0,
 \end{aligned}$$

for the unknown function $u : \Omega \times \Sigma \rightarrow \mathbb{R}$. The scalar, vector and matrix-valued coefficients $c(\mathbf{x}, t)$, $\mathbf{b}(\mathbf{x}, t)$ and $D(\mathbf{x}, t)$ are understood as functions of a spatial variable $\mathbf{x} \in \Omega$ and time $t \in \Sigma$, $\boldsymbol{\nu}(\mathbf{x})$ is the unit outer normal vector. $D(\mathbf{x}, t)$ is symmetric, uniformly positive definite and may be discontinuous (with discontinuities resolved by the computational mesh). The velocity field $\mathbf{b}(\mathbf{x}, t)$ is assumed to be in $H(\text{div}; \Omega)$ for fixed t . The outflow boundary condition (1d) is only used in the convection-dominated case and it is assumed that $\Gamma_O \subseteq \Gamma^+ = \{\mathbf{x} \in \partial\Omega : \mathbf{b}(\mathbf{x}) \cdot \boldsymbol{\nu}(\mathbf{x}) \geq 0\}$. Below we will also consider the stationary variant of equation (1) where $\partial_t u = 0$, all coefficients depend only on space and the initial condition (1e) is omitted. This model problem occurs (at least as a component) in a wide range of applications such as heat and fluid flow or computational biology. We are particularly interested in porous media flow where (variants of) equation (1) model the flow of one or several fluid phases possibly coupled with transport of dissolved substances [5, 30, 35]. One difficulty of flows in porous media is that coefficients \mathbf{b} and D are highly varying in space and time.

2.2. Discontinuous Galerkin Discretization. As spatial discretization of equation (1) we employ the weighted symmetric interior penalty discontinuous Galerkin (WSIPG) method introduced in [24]. This method is attractive as it is locally mass conservative, works on very general meshes, allows varying polynomial degree, can handle highly varying, anisotropic and matrix-valued diffusion coefficients [4] and is also suited for the convection-dominated case [38]. $H(\operatorname{div}; \Omega)$ flow fields, if required, can be reconstructed locally by means of interpolation [25, 11].

Let $\{\mathcal{T}_h\}_{h>0}$ be a family of shape regular triangulations of the domain Ω consisting of closed elements T , each being the image of a map $\mu_T : \hat{T} \rightarrow T$ with \hat{T} the reference cube in d dimensions. The map μ_T is differentiable, invertible and its gradient is nonsingular on \hat{T} . The diameter of T is h_T and $\boldsymbol{\nu}_T$ is its unit outer normal vector. F is an interior face if it is the intersection of two elements $T^-(F), T^+(F) \in \mathcal{T}_h$ and F has non-zero $d-1$ -dimensional measure. All interior faces are collected in the set \mathcal{F}_h^i . Likewise, F is a boundary face if it is the intersection of some $T^-(F) \in \mathcal{T}_h$ with $\partial\Omega$ and has non-zero $d-1$ -dimensional measure. All boundary faces make up the set $\mathcal{F}_h^{\partial\Omega} = \mathcal{F}_h^D \cup \mathcal{F}_h^N \cup \mathcal{F}_h^O$ (subdivided into Dirichlet, Neumann and outflow boundary faces) and we set $\mathcal{F}_h = \mathcal{F}_h^i \cup \mathcal{F}_h^{\partial\Omega}$. The diameter of $F \in \mathcal{F}_h$ is h_F and with each $F \in \mathcal{F}_h$ we associate a unit normal vector $\boldsymbol{\nu}_F$ oriented from $T^-(F)$ to $T^+(F)$ in case of interior faces and coinciding with the unit outer normal to Ω in case of boundary faces. Every face F is the image of a map $\mu_F : \hat{F} \rightarrow F$ with \hat{F} the reference element of the face.

The DG finite element space of degree p on the mesh \mathcal{T}_h is then

$$(2) \quad V_h^p = \{v \in L^2(\Omega) : \forall T \in \mathcal{T}_h, v|_T = q \circ \mu_T^{-1} \text{ with } q \in \mathbb{Q}_p^d\}$$

where \mathbb{Q}_p^d is the set of polynomials of maximum degree p in dimension d (all methods presented could be generalized to varying polynomial degree per direction and also per cell). A function $v \in V_h^p$ is two-valued on an interior face $F \in \mathcal{F}_h^i$ and by v^- we denote the restriction from $T^-(F)$ and by v^+ the restriction from $T^+(F)$. For any point $\mathbf{x} \in F \in \mathcal{F}_h^i$ we define jump and weighted average as

$$\llbracket v \rrbracket(\mathbf{x}) = v^-(\mathbf{x}) - v^+(\mathbf{x}), \quad \{v\}_\omega(\mathbf{x}) = \omega^-(\mathbf{x})v^-(\mathbf{x}) - \omega^+(\mathbf{x})v^+(\mathbf{x})$$

for weights $\omega^-(\mathbf{x}) + \omega^+(\mathbf{x}) = 1$, $\omega^\pm(\mathbf{x}) \geq 0$. A particular choice of the weights depending on the diffusion coefficient D has been introduced in [17, 26]:

$$\omega^-(\mathbf{x}) = \frac{\delta_{D\nu}^+(\mathbf{x})}{\delta_{D\nu}^-(\mathbf{x}) + \delta_{D\nu}^+(\mathbf{x})}, \quad \omega^+(\mathbf{x}) = \frac{\delta_{D\nu}^-(\mathbf{x})}{\delta_{D\nu}^-(\mathbf{x}) + \delta_{D\nu}^+(\mathbf{x})}$$

with $\delta_{D\nu}^\pm(\mathbf{x}) = \boldsymbol{\nu}^T(\mathbf{x})D^\pm(\mathbf{x})\boldsymbol{\nu}(\mathbf{x})$. The definitions of jump and average are extended to boundary points $\mathbf{x} \in F \in \mathcal{F}_h^{\partial\Omega}$ by

$$\llbracket v \rrbracket(\mathbf{x}) = \{v\}_\omega(\mathbf{x}) = v^-(\mathbf{x}).$$

Finally, we denote for any domain Q by

$$(v, w)_Q = \int_Q v \cdot w \, dx$$

the L^2 scalar product of two (possibly vector-valued) functions, by $|Q| = (1, 1)_Q$ the measure of the set Q and by $\langle a, b \rangle = 2ab/(a+b)$ the harmonic mean of two numbers.

Following the method of lines paradigm we first discretize equation (1) in space using the WSIPG method. This leads to the discrete in space, continuous in time problem

$$(3) \quad u_h(t) \in V_h^p : \quad \frac{d}{dt}(u_h(t), v)_\Omega + a_h(u_h(t), v; t) = l_h(v; t) \quad \forall v \in V_h^p, t \in \Sigma,$$

with the bilinear form

$$(4) \quad \begin{aligned} a_h(u, v; t) = & \sum_{T \in \mathcal{T}_h} [(D\nabla u - \mathbf{b}u, \nabla v)_T + (cu, v)_T] + \sum_{F \in \mathcal{F}_h^i} (\Phi(u^-, u^+, \boldsymbol{\nu}_F \cdot \mathbf{b}), \llbracket v \rrbracket)_F \\ & + \sum_{F \in \mathcal{F}_h^{pO}} (\Phi(u, 0, \boldsymbol{\nu}_F \cdot \mathbf{b}), v)_F - \sum_{F \in \mathcal{F}_h^{iD}} (\boldsymbol{\nu}_F \cdot \{D\nabla u\}_\omega, \llbracket v \rrbracket)_F \\ & - \sum_{F \in \mathcal{F}_h^{iD}} (\boldsymbol{\nu}_F \cdot \{D\nabla v\}_\omega, \llbracket u \rrbracket)_F + \sum_{F \in \mathcal{F}_h^{iD}} \gamma_F(\llbracket u \rrbracket, \llbracket v \rrbracket)_F \end{aligned}$$

and the right hand side functional

$$(5) \quad \begin{aligned} l_h(v; t) = & \sum_{T \in \mathcal{T}_h} (f, v)_T - \sum_{F \in \mathcal{F}_h^N} (j, v)_F ds - \sum_{F \in \mathcal{F}_h^D} (\Phi(0, g, \boldsymbol{\nu}_F \cdot \mathbf{b}), v)_F \\ & - \sum_{F \in \mathcal{F}_h^D} (\boldsymbol{\nu}_F \cdot (D\nabla v), g)_F ds + \sum_{F \in \mathcal{F}_h^D} \gamma_F(g, v)_F. \end{aligned}$$

Here we adopted the notation $\mathcal{F}_h^{AB} = \mathcal{F}_h^A \cup \mathcal{F}_h^B$. The penalty factor γ_F is chosen as

$$\gamma_F = \alpha \langle \delta_{D\nu_F}^-, \delta_{D\nu_F}^+ \rangle M, \quad M = p(p+d-1) \frac{|F|}{\min(|T^-(F)|, |T^+(F)|)}$$

where α is a free parameter typically chosen to be $\alpha = 2$. This formulation employs the upwind flux on the face which is given by

$$\Phi(u^-, u^+, b_\nu) = \begin{cases} u^- b_\nu & b_\nu \geq 0 \\ u^+ b_\nu & \text{else} \end{cases},$$

where we denote by $b_\nu = \mathbf{b} \cdot \boldsymbol{\nu}$ the normal flux. It is helpful to split the bilinear form (4) into volume, interior face and boundary face contributions:

$$(6) \quad a_h(u, v; t) = \sum_{T \in \mathcal{T}_h} a_{\Omega, T}(u, v; t) + \sum_{F \in \mathcal{F}_h^i} a_{i, F}(u, v; t) + \sum_{F \in \mathcal{F}_h^{\partial\Omega}} a_{\partial\Omega, F}(u, v; t)$$

A similar decomposition can be done for the right hand side.

Upon choosing a basis of the finite element space $V_h^p = \text{span}\{\phi_1, \dots, \phi_{N_h}\}$ the discrete in space problem (3) is equivalent to solving a system of ordinary differential equations

$$(7) \quad M_h \frac{dz_h(t)}{dt} + A_h(t) z_h(t) = f_h(t)$$

for the unknown coefficients $z_h(t)$ in the expansion $u_h(t) = \sum_{j=1}^{N_h} (z_h(t))_j \phi_j$. The mass matrix M_h , system matrix $A_h(t)$ and the right hand side vector $f_h(t)$ have the entries

$$(M_h)_{i,j} = (\phi_j, \phi_i)_\Omega, \quad (A_h(t))_{i,j} = a_h(\phi_j, \phi_i; t), \quad (f_h(t))_i = l_h(\phi_i; t).$$

A prominent advantage of DG is that the basis can be chosen such that M_h is block diagonal or even diagonal which simplifies the implementation of explicit time-stepping methods significantly.

For the time discretization of (7) we use strong stability preserving explicit Runge-Kutta methods [45, 16]. E.g. one step of the explicit Euler method reads

$$M_h z_h^{(k+1)} = M_h z_h^{(k)} + \Delta t \left(f_h(t^{(k)}) - A_h(t^{(k)}) z_h^{(k)} \right).$$

Higher-order Runge-Kutta methods involve basically the same computations per stage. Since we use L_2 -orthogonal Legendre Polynomials the mass matrix M_h is diagonal in our case. Below we focus first on the matrix-free computation of $y_h = A_h z_h$ (silently dropping the time index here) and then on the computation of a complete step of the explicit Runge-Kutta method.

3. Sum-Factorization for Discontinuous Galerkin Methods.

3.1. Tensor Product Finite Element Functions. On a given element $T \in \mathcal{T}_h$ a finite element function $u_h \in V_h^p$ can be expressed as $u_h(x) = \sum_{j \in J} z_{g(T,j)} \hat{\phi}_j(\mu_T^{-1}(x))$ where the $\hat{\phi}_j$ are the $|J|$ shape functions on the reference element \hat{T} spanning the polynomials in \mathbb{Q}_p^d and $g: \mathcal{T}_h \times J \rightarrow \{1, \dots, N_h\}$ is the map associating local numbers of shape functions with numbers of global basis functions. Note that in discontinuous Galerkin one typically chooses global basis functions that have support in only one element.

The main assumption for the rest of the paper is that the shape functions have tensor product structure,

$$(8) \quad \hat{\phi}_j(\hat{\mathbf{x}}) = \hat{\phi}_{(j_1, \dots, j_d)}(\hat{x}_1, \dots, \hat{x}_d) = \prod_{k=1}^d \hat{\theta}_{j_k}^{(k)}(\hat{x}_k)$$

where $\mathbf{J} = J^{(1)} \times \dots \times J^{(d)}$, $J^{(k)} = \{1, \dots, n_k\}$, consists of d -tuples enumerating the shape functions and $\hat{\theta}_{j_k}^{(k)}$ is the one-dimensional basis function number j_k in direction k on the reference element. In principle, the one-dimensional basis can be different for every direction and a different basis can be chosen for each element (anisotropic hp -refinement). In our implementation, however, it is currently the same in all directions for all elements, i.e. $n_1 = \dots = n_d = n$.

For the numerical evaluation of integrals quadrature of appropriate order is used:

$$(9) \quad \int_{\hat{T}} f(\hat{\mathbf{x}}) d\hat{\mathbf{x}} = \sum_{i_1 \in I_1} \dots \sum_{i_d \in I_d} f(\xi_{i_1}^{(1)}, \dots, \xi_{i_d}^{(d)}) w_{(i_1, \dots, i_d)} + \text{error}.$$

Here, the quadrature formula with points $\boldsymbol{\xi}_i = (\xi_{i_1}^{(1)}, \dots, \xi_{i_d}^{(d)})$ and weights $w_i = w_{(i_1, \dots, i_d)} = \prod_{k=1}^d w_{i_k}^{(k)}$ has tensor product form. The $\xi_{i_k}^{(k)}$ with weights $w_{i_k}^{(k)}$ are one-dimensional quadrature points and weights for direction k with $i_k \in I^{(k)} = \{1, \dots, m_k\}$. $\mathbf{I} = I^{(1)} \times \dots \times I^{(d)}$ is the index set of all quadrature points. Again, quadrature order could be chosen per element and direction but in our implementation we assume $m_1 = \dots = m_d = m$ (but *not* necessarily $m = n$).

3.2. Weak Form Evaluation. Evaluation of the weak form (4) requires the computation of element-wise integrals. We now consider the part of the volume integral on element $T \in \mathcal{T}_h$ in detail for a given test function ϕ_k with $k = g(T, \mathbf{j})$, $\mathbf{j} \in \mathbf{J}$:

$$\begin{aligned}
(10) \quad & (D\nabla u - \mathbf{b}u, \nabla\phi_k)_T \\
&= \int_T (D(\mathbf{x})\nabla u - \mathbf{b}(\mathbf{x})u) \cdot \nabla\phi_k \, dx \\
&= \int_{\hat{T}} \left(D(\mu_T(\hat{\mathbf{x}}))\hat{S}_T(\hat{\mathbf{x}})\hat{\nabla}\hat{u}(\hat{\mathbf{x}}) - \mathbf{b}(\mu_T(\hat{\mathbf{x}}))\hat{u}(\hat{\mathbf{x}}) \right) \cdot \left(\hat{S}_T(\hat{\mathbf{x}})\hat{\nabla}\hat{\phi}_j(\hat{\mathbf{x}}) \right) \Delta_T(\hat{\mathbf{x}}) \, dx \\
&\approx \sum_{\mathbf{i} \in I} \left(\hat{D}(\boldsymbol{\xi}_i)\hat{\nabla}\hat{u}(\boldsymbol{\xi}_i) - \hat{\mathbf{b}}(\boldsymbol{\xi}_i)\hat{u}(\boldsymbol{\xi}_i) \right) \cdot \hat{\nabla}\hat{\phi}_j(\boldsymbol{\xi}_i)\Delta_T(\boldsymbol{\xi}_i)w_i \\
&= \sum_{i_1 \in I^{(1)}} \dots \sum_{i_d \in I^{(d)}} \sum_{r=1}^d \hat{\partial}_r \hat{\phi}_j(\boldsymbol{\xi}_i) \left[\left(\sum_{s=1}^d \hat{D}_{r,s}(\boldsymbol{\xi}_i)\hat{\partial}_s \hat{u}(\boldsymbol{\xi}_i) - \hat{b}_r(\boldsymbol{\xi}_i)\hat{u}(\boldsymbol{\xi}_i) \right) \Delta_T(\boldsymbol{\xi}_i)w_i \right] \\
&= \sum_{r=1}^d \sum_{i_1 \in I^{(1)}} \dots \sum_{i_d \in I^{(d)}} \hat{\partial}_r \left(\hat{\theta}_{j_1}^{(1)}(\boldsymbol{\xi}_{i_1}) \dots \hat{\theta}_{j_d}^{(d)}(\boldsymbol{\xi}_{i_d}) \right) \\
&\quad \left[\left(\sum_{s=1}^d \hat{D}_{r,s}(\boldsymbol{\xi}_i)\hat{\partial}_s \hat{u}(\boldsymbol{\xi}_i) - \hat{b}_r(\boldsymbol{\xi}_i)\hat{u}(\boldsymbol{\xi}_i) \right) \Delta_T(\boldsymbol{\xi}_i)w_i \right] \\
&= \sum_{r=1}^d \sum_{i_1 \in I^{(1)}} \dots \sum_{i_d \in I^{(d)}} A_{j_1, i_1}^{(1,r)} \dots A_{j_d, i_d}^{(d,r)} x_{(i_1, \dots, i_d)}^{(r)}
\end{aligned}$$

where now

$$(11) \quad A_{\alpha, \beta}^{(q,r)} = \begin{cases} \frac{d\hat{\theta}_\alpha^{(q)}}{d\hat{\mathbf{x}}}(\boldsymbol{\xi}_\beta^{(q)}) & q = r \\ \hat{\theta}_\alpha^{(q)}(\boldsymbol{\xi}_\beta^{(q)}) & \text{else} \end{cases}, \quad \alpha \in J^{(q)}, \beta \in I^{(q)},$$

are small matrices which contain the values of the (derivative of) the one-dimensional basis functions at the one-dimensional quadrature points per direction and

$$(12) \quad x_i^{(r)} = \left(\sum_{s=1}^d \hat{D}_{r,s}(\boldsymbol{\xi}_i)\hat{\partial}_s \hat{u}(\boldsymbol{\xi}_i) - \hat{b}_r(\boldsymbol{\xi}_i)\hat{u}(\boldsymbol{\xi}_i) \right) \Delta_T(\boldsymbol{\xi}_i)w_i$$

are quantities to be computed at every quadrature point involving values of (the derivatives of) the finite element function u on the element, the coefficients of the PDE and the geometry of the element T .

In (10) we use $\hat{S}_T(\hat{\mathbf{x}}) = (\nabla\mu_T(\hat{\mathbf{x}}))^{-T}$ in order to transform gradients from the reference element to the real element, set $\hat{D}(\hat{\mathbf{x}}) = \hat{S}_T^T(\hat{\mathbf{x}})D(\mu_T(\hat{\mathbf{x}}))\hat{S}_T(\hat{\mathbf{x}})$, $\hat{\mathbf{b}}(\hat{\mathbf{x}}) = \hat{S}_T^T(\hat{\mathbf{x}})\mathbf{b}(\mu_T(\hat{\mathbf{x}}))$ and abbreviate $\Delta_T(\hat{\mathbf{x}}) = |\det \hat{\nabla}\mu_T(\hat{\mathbf{x}})|$.

We remark that (10) remains valid for nonlinear PDEs as well as high-order geometry transformations. Only the tensor product structure of quadrature and test functions as well as linearity in the test function is used.

3.3. Finite Element Function Evaluation. Equation (12) requires the evaluation of a finite element function and its gradient at all quadrature points in an

element $T \in \mathcal{T}_h$. We demonstrate the function evaluation:

$$\begin{aligned}
(13) \quad \hat{u}(\boldsymbol{\xi}_i) &= \sum_{j \in J} z_{g(T,j)} \hat{\phi}_j(\boldsymbol{\xi}_i) \\
&= \sum_{j_1 \in J^{(1)}} \dots \sum_{j_d \in J^{(d)}} \hat{\theta}_{j_1}^{(1)}(\boldsymbol{\xi}_{i_1}^{(1)}) \cdot \dots \cdot \hat{\theta}_{j_d}^{(d)}(\boldsymbol{\xi}_{i_d}^{(d)}) z_{g(T,(j_1, \dots, j_d))} \\
&= \sum_{j_1 \in J^{(1)}} \dots \sum_{j_d \in J^{(d)}} A_{i_1, j_1}^{(1)} \cdot \dots \cdot A_{i_d, j_d}^{(d)} x_{(j_1, \dots, j_d)}.
\end{aligned}$$

With $A_{\alpha, \beta}^{(q)} = \theta_{\beta}^{(q)}(\boldsymbol{\xi}_{\alpha}^{(q)})$, $\alpha \in I^{(q)}$, $\beta \in J^{(q)}$ and $x_{(j_1, \dots, j_d)} = z_{g(T,(j_1, \dots, j_d))}$ this computation has the same structure as that in (10). The gradient can be evaluated in a similar fashion and involves the matrices $(A^{(q,r)})^T$ from (11).

3.4. Face Integral Evaluation. Some more notation is needed to describe the evaluation of face integrals. The embedding of face F into $T^{\pm}(F)$ is described by maps $\eta_F^{\pm} : \hat{F} \rightarrow \hat{T}$ of the corresponding reference elements such that $\mu_{T^{\pm}(F)}(\eta_F^{\pm}(\hat{\mathbf{x}})) = \mu_F(\hat{\mathbf{x}})$ holds. The maps η_F^{\pm} map coordinate number $q \in \{1, \dots, d-1\}$ in \hat{F} to coordinate number $\pi_F^{\pm}(q)$ in \hat{T} and correspondingly $T^{\pm}(F)$. By $q_F^{\pm} \in \{1, \dots, d\}$ we denote the unique coordinate number that face \hat{F} is perpendicular to in the corresponding \hat{T} and we may formally *extend* the map π_F^{\pm} to $\{1, \dots, d\}$ by setting $\pi_F^{\pm}(d) = q_F^{\pm}$ (so π_F^{\pm} is a permutation of $\{1, \dots, d\}$). Finally, since faces in the volume reference element are axi-parallel, the component $(\eta_F^{\pm}(\hat{\mathbf{x}}))_{\pi_F^{\pm}(q)} = \eta_{F, \pi_F^{\pm}(q)}^{\pm}(\hat{x}_q)$ is a function of one argument only and in the case of conforming refinement it is even an isometry.

For illustration we now consider the interior penalty term on face $F \in \mathcal{F}_h^i$ evaluated for a test function ϕ_k with support on $T^-(F)$ and $k = g(T^-(F), \mathbf{j})$, $\mathbf{j} \in \mathbf{J}$.

$$\begin{aligned}
(14) \quad ([u], [\phi_k])_F &= \int_F \llbracket u(\mathbf{x}) \rrbracket \phi_k(\mathbf{x}) dx = \int_{\hat{F}} \llbracket u(\mu_F(\hat{\mathbf{x}})) \rrbracket \hat{\phi}_j(\eta_F^-(\hat{\mathbf{x}})) \Delta_F(\hat{\mathbf{x}}) dx \\
&\approx \sum_{i_1 \in I^{(1)}} \dots \sum_{i_{d-1} \in I^{(d-1)}} \hat{\theta}_{j_{\pi_F^-(1)}}^{(\pi_F^-(1))} \left(\eta_{F, \pi_F^-(1)}^-(\boldsymbol{\xi}_{i_1}^{(1)}) \right) \cdot \dots \cdot \hat{\theta}_{j_{\pi_F^-(d-1)}}^{(\pi_F^-(d-1))} \left(\eta_{F, \pi_F^-(d-1)}^-(\boldsymbol{\xi}_{i_{d-1}}^{(d-1)}) \right) \\
&\quad \hat{\theta}_{j_{q_F^-}}^{(q_F^-)} \left(\eta_{F, q_F^-}^-(0) \right) \llbracket \hat{u}(\eta_F^-(\boldsymbol{\xi}_i)) \rrbracket \Delta_F(\boldsymbol{\xi}_i) w_i \\
&= \sum_{i_1 \in I^{(1)}} \dots \sum_{i_{d-1} \in I^{(d-1)}} \sum_{i_d \in I^{(d)}} B_{j_{\pi_F^-(1)}, i_1}^{(1)} \cdot \dots \cdot B_{j_{\pi_F^-(d-1)}, i_{d-1}}^{(d-1)} B_{j_{q_F^-}, i_d}^{(d)} x_{(i_1, \dots, i_d)}.
\end{aligned}$$

where we formally introduced the one element index set $I^{(d)} = \{1\}$ and defined the matrices

$$B_{\alpha, \beta}^{(q)} = \begin{cases} \hat{\theta}_{\alpha}^{(\pi_F^-(q))} \left(\eta_{F, \pi_F^-(q)}^-(\boldsymbol{\xi}_{\beta}^{(q)}) \right) & 1 \leq q < d, \alpha \in J^{(\pi_F^-(q))}, \beta \in I^{(q)} \\ \hat{\theta}_{\alpha}^{(q_F^-)} \left(\eta_{F, q_F^-}^-(0) \right) & q = d, \alpha \in J^{(\pi_F^-(q))}, \beta = 1 \end{cases}$$

as well as the coefficients

$$x_i = x_{(i_1, \dots, i_d)} = \llbracket \hat{u}(\eta_F^-(\boldsymbol{\xi}_{i_1}^{(1)}, \dots, \boldsymbol{\xi}_{i_{d-1}}^{(d-1)})) \rrbracket \Delta_F(\boldsymbol{\xi}_{i_1}^{(1)}, \dots, \boldsymbol{\xi}_{i_{d-1}}^{(d-1)}) w_{i_1, \dots, i_{d-1}}.$$

Note that $\eta_{F, q_F^-}^-(0) \in \{0, 1\}$ is independent of its argument since the face is perpendicular to direction q_F^- and therefore we can supply a dummy argument.

Structurally we obtain the same expression as for the evaluation of the volume integral. Similar to section 3.3 it can be shown that evaluation of the finite element functions from both sides on a face leads to a similar expression now involving the transposed of the matrices $B^{(q)}$.

3.5. Sum Factorization. (13) Subsections 3.2, 3.3 and 3.4 demonstrate that finite element function evaluation and computation of finite element integrals all lead to the same abstract structure (e.g. compare to equation (13)):

$$(15) \quad y_{(i_1, \dots, i_d)} = \sum_{j_1 \in J^{(1)}}^{n_1} \dots \sum_{j_d \in J^{(d)}}^{n_d} A_{i_1, j_1}^{(1)} \dots A_{i_d, j_d}^{(d)} x_{(j_1, \dots, j_d)}$$

for all indices $(i_1, \dots, i_d) \in I^{(1)} \times \dots \times I^{(d)}$. Assuming that $|I^{(q)}| = m$ and $|J^{(q)}| = n$ for all $q \in \{1, \dots, d\}$ and $n/m = \rho \leq 1$ (number of quadrature points is not smaller than number of basis functions per direction) the cost for naive evaluation of the expression (15) is

$$\text{Cost}_{naive} = (d+1)\rho^d m^{2d} \text{ flops.}$$

A substantial reduction in the computational cost can be achieved with the *dimension by dimension* or *sum factorization* algorithm [39, 12, 37] based on extracting common factors in the sums:

$$\begin{aligned} y_{(i_1, \dots, i_d)} &= \sum_{j_d \in J^{(d)}} \dots \sum_{j_1 \in J^{(1)}} A_{i_d, j_d}^{(d)} \dots A_{i_1, j_1}^{(1)} x_{(j_1, \dots, j_d)} \\ &= \sum_{j_d \in J^{(d)}} \dots \sum_{j_2 \in J^{(2)}} A_{i_d, j_d}^{(d)} \dots A_{i_2, j_2}^{(2)} \sum_{j_1 \in J^{(1)}} A_{i_1, j_1}^{(1)} x_{(j_1, \dots, j_d)} \\ &= \sum_{j_d \in J^{(d)}} \dots \sum_{j_2 \in J^{(2)}} A_{i_d, j_d}^{(d)} \dots A_{i_2, j_2}^{(2)} z_{(i_1, j_2, \dots, j_d)}^{(1)} \\ &= \sum_{j_d \in J^{(d)}} \dots \sum_{j_3 \in J^{(3)}} A_{i_d, j_d}^{(d)} \dots A_{i_3, j_3}^{(3)} \sum_{j_2 \in J^{(2)}} A_{i_2, j_2}^{(2)} z_{(i_1, j_2, \dots, j_d)}^{(1)} \\ &= \sum_{j_d \in J^{(d)}} \dots \sum_{j_3 \in J^{(3)}} A_{i_d, j_d}^{(d)} \dots A_{i_3, j_3}^{(3)} z_{(i_1, i_2, j_3, \dots, j_d)}^{(2)} = \dots \\ &= \sum_{j_d \in J^{(d)}} A_{i_d, j_d}^{(d)} z_{(i_1, \dots, i_{d-1}, j_d)}^{(d-1)} = z_{(i_1, \dots, i_d)}^{(d)}. \end{aligned}$$

Per direction, the *sum factorization kernel*

$$(16) \quad z_{(i_1, \dots, i_q, j_{q+1}, \dots, j_d)}^{(q)} = \sum_{j_q \in J^{(q)}} A_{i_q, j_q}^{(q)} z_{(i_1, \dots, i_{q-1}, j_q, \dots, j_d)}^{(q-1)}, \quad \forall i_q \in I^{(q)},$$

needs to be carried out, where $z^{(0)} = x$. The computation in (16) can be viewed as a matrix-matrix product (albeit of rather small matrices) when $z^{(q-1)}$ is stored as a matrix with j_{q-1} as row index and the product of the other indices as column index [12]. In order to facilitate recursive application, the output $z^{(q)}$ needs to be stored such that j_q is the new row index, which can be interpreted as a tensor rotation of the output. If the matrix-matrix product is implemented with the columns of z^{q-1} as the slowest index and if the tensor rotation is fused into the matrix-matrix product kernel, the resulting computation reads $z^{(q-1)}$ sequentially and writes $z^{(q)}$ sequentially, which

ensures optimal memory transfer bandwidths. Counting now the number of floating point operations yields

$$(17) \quad \text{Cost}_{vol}(d, m, \rho) = 2C_{d,\rho}m^{d+1}$$

for volume terms and

$$(18) \quad \text{Cost}_{face}(d, m, \rho) = 2C_{d,\rho}m^d$$

for face terms where we set

$$C_{d,\rho} = \sum_{q=1}^d \rho^q = \begin{cases} \rho \frac{1-\rho^d}{1-\rho} & \rho < 1 \\ d & \rho = 1 \end{cases}.$$

Note that in contrast to the naive evaluation all operations are fused-multiply-add operations due to the matrix-matrix products. Achieving the optimal cost for face terms (18) requires processing the direction q_F^\pm as *first* direction when evaluating a finite element function at quadrature points or as *last* direction when computing face integrals for all test functions. For moderate polynomial degrees (say $p \leq 6$) the cost for the face terms will dominate. In that case the cost per degree of freedom will be independent of the polynomial degree since the number of degrees of freedom per element is $n^d = O(m^d)$.

3.6. Matrix-free Finite Element Operator Application. The application of the finite element operator refers to evaluate, for a given $u_h \in V_h^p$, the bilinear form $a(u_h, \phi)$ for all basis functions ϕ spanning the finite element space V_h^p . As an extension of [34] this operation can be performed in a matrix-free setting by the following algorithm using three steps per mesh entity: The computational complexity

Algorithm 1 Matrix-free operator evaluation.

for $T \in \mathcal{T}_h$ **do**

(1) Compute $\hat{u}_h, \hat{\nabla} \hat{u}_h$ for all quadrature points on corresponding \hat{T}

(2) Compute coefficients at all quadrature points

(3) Compute $a_{\Omega,T}(u_h, \phi)$ for all basis functions ϕ with support on T

for $F \in \mathcal{F}_h^i \cap \partial T$ and F not treated yet **do**

(4) Compute $\hat{u}_h^-, \hat{u}_h^+, \hat{\nabla} \hat{u}_h^-, \hat{\nabla} \hat{u}_h^+$ for all quadrature points on corresp. \hat{F}

(5) Compute coefficients at all quadrature points

(6) Compute $a_{i,F}(u_h, \phi^\mp)$ for all ϕ^-, ϕ^+ with support on $T^-(F), T^+(F)$

(7) Mark F as treated

end for

for $F \in \mathcal{F}_h^{\partial\Omega} \cap \partial T$ **do**

(8) Compute $\hat{u}_h^-, \hat{\nabla} \hat{u}_h^-$ for all quadrature points on corresponding \hat{F}

(9) Compute coefficients at all quadrature points

(10) Compute $a_{\partial\Omega,F}(u_h, \phi)$ for all basis functions ϕ with support on T

end for

end for

of steps (1) and (3) of the algorithm is given in (17), the computational complexity of steps (4), (6), (8) and (10) of the algorithm is given by (18) while the computational complexity of the remaining steps (2), (5) and (9) is proportional to the number of quadrature points.

Based on the cost of the volume and face sum factorization kernels (17) and (18) we can estimate the total cost for a full operator evaluation. For the case $n = m = p + 1$, constant full diffusion tensor, constant velocity field and affine element transformation we obtain the following lower bound on the number of floating point operations per degree of freedom (FLOPDOF) depending on polynomial degree p and space dimension d :

$$(19) \quad \text{FLOPDOF}_{vol}(d, p) = 4(d + 1)d(p + 1) + 2d^2 + 5d + 3,$$

$$(20) \quad \text{FLOPDOF}_{face}(d, p) = 8(d + 1)d^2 + d(2d^2 + 8d + 18)(p + 1)^{-1}.$$

Here we estimate the computational effort at each quadrature point by $2d^2 + 5d + 3$. The amount of data transferred (in Bytes) per degree of freedom (BDOF) can be estimated as:

$$(21) \quad \text{BDOF}_{vol}(d, p) = 16, \quad \text{BDOF}_{face}(d, p) = 32d,$$

where we assumed that all temporary variables fit into cache and only coefficients and result need to be transferred from/to memory. Note that face computations are more memory-intense since there are d faces per element on average and for each face we read/write data for both adjacent elements.

The roofline model predicts the achievable performance in GFLOPs/s from the given peak performance π (in GFLOPs/s) and memory bandwidth β (in GB/s) of the system as well as the theoretically determined compute intensities

$$I_{vol}(d, p) = \frac{\text{FLOPDOF}_{vol}(d, p)}{\text{BDOF}_{vol}(d, p)}, \quad I_{face}(d, p) = \frac{\text{FLOPDOF}_{face}(d, p)}{\text{BDOF}_{face}(d, p)},$$

of the algorithm as

$$P = \min(\pi, \beta I).$$

Plotting the predicted performance P over the compute intensity I gives the roofline plot in Figure 2. It shows that the algorithm is fully compute bound except for face terms in two space dimensions. For comparison we include also matrix-based matrix vector multiplication which has a compute intensity of $I_{matmul} = 1/4$ and performs at 3,75 GFLOPs/s.

Assuming now that $3d$ computations are compute-bound for all polynomial degrees we obtain the theoretical throughput (TPUT) in degrees of freedom (DOFs) processed per second on a full node consisting of two Xeon E5-2698v3 2.3 GHz processors (with 32 cores in total) as

$$\text{TPUT}(d, p) = \frac{32\pi}{\text{FLOPDOF}_{vol}(d, p) + \text{FLOPDOF}_{face}(d, p)}.$$

For $d = 3$ compute intensity and throughput are shown in Figure 3. Corresponding experimental results will be shown in Section 5 below.

4. Implementation Issues. We have realized the numerical scheme outlined in the previous section within the PDELab [10] finite element framework which is based on the Dune software framework [6]. Within the EXA-DUNE project [9] the Dune software framework is currently being prepared for current and future HPC architectures. By design, Dune and PDELab are very general and allow for different mesh types and general discretizations. This flexibility sacrifices, to some extent, performance for generality and in order to obtain a high-performance implementation of

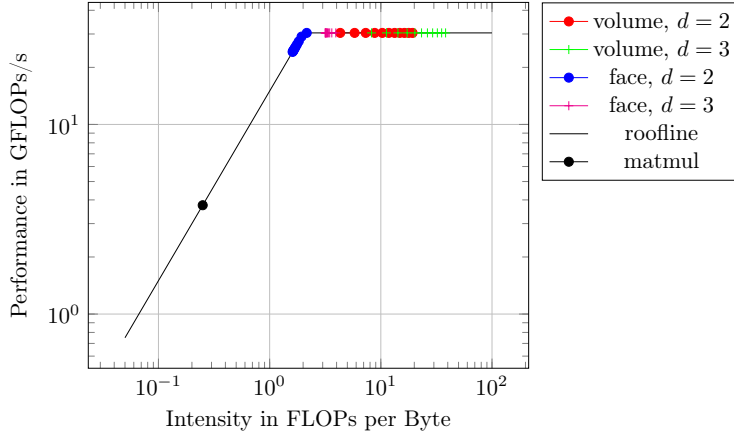


FIG. 2. Roofline plot for one Intel Xeon E5-2698v3 2.3 GHz core with the following hardware characteristics: $\beta = 15$ GB/s, $\pi = 30,4$ GFLOPs/s.

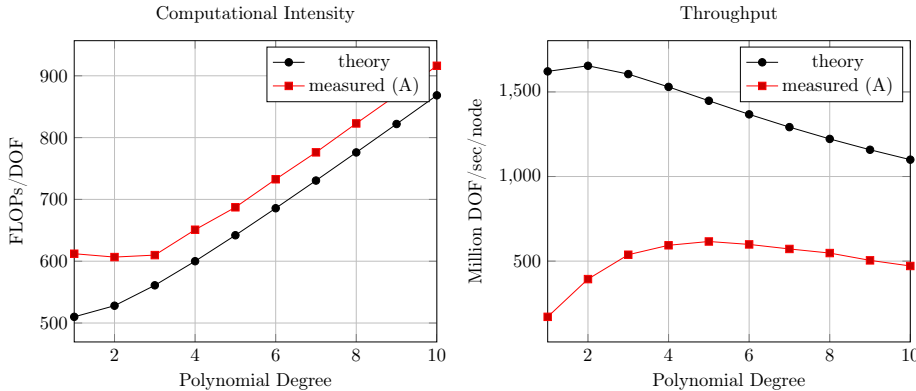


FIG. 3. Theoretical compute intensity and throughput for a 3d computation on an axiparallel mesh with constant diffusion tensor assuming $\pi = 32 \cdot 30,4$ GFLOPs/s for the full node.

sum factorized DG assembly, we had to redesign parts of the underlying framework. In this Section, we will focus on two different aspects that were crucial for the performance of our code: the vectorization strategy to exploit SIMD parallelism of modern CPU architectures and the block structure of DG vectors that can be used to reduce the amount of memory transfers.

Peak performance of modern many-core CPUs can only be achieved with SIMD vector instructions. Here we are concerned with Intel Haswell processors offering the AVX2 instruction set which operates on four double-precision floating point numbers in parallel. Although matrix-matrix multiplication of sufficiently large matrices vectorizes very well, the small size of the matrices involved in sum factorization is a challenge. For example, a single step of the sum-factorization algorithm given by equation (16) in three dimensions for polynomial degree three involves the product of a 4×4 and a 4×16 matrix. While the performance for multiplication of small matrices is meanwhile addressed on a library level by `libxsmm` [29] we provide our own implementation based on the following principles:

- i) Increase size of the matrices by collecting several sum factorization steps. The

FMA instructions in current Intel processors have a latency of 4-5 processor cycles and the processor can issue two such instructions per cycle. Therefore one requires 8-10 independent summation chains of 4 values each to fully exploit the floating point performance of the processor.

- ii) Aim at at least one matrix dimension being a multiple of the SIMD vector unit (four here).
- iii) Arrange the output matrix of the matrix-matrix product in a way that enables recursive application of the steps (16) and avoid a separate tensor rotation. This results in a non-standard matrix-matrix product which is currently not available in the `libxsmm` library at the time of writing.

There are several ways to increase the amount of work as stated in principle i). One option is to work simultaneously on k cells or facets where k is the SIMD width ($k = 4$ in our case). This has the advantage of producing an innermost loop of size k and vectorization is independent of polynomial degree, quadrature order and spatial dimension. On the other hand the data of k cells needs to be accessed simultaneously which puts more pressure on the cache for larger polynomial degrees.

Another option, which we have chosen in this work, is to exploit the fact that the finite element method applied to second order PDEs involves functions as well as their gradients and to work on just one element or facet at a time. This is particularly appealing in three spatial dimensions for AVX2, where we can group together the four values $[\partial_{x_1} u(\boldsymbol{\xi}), \partial_{x_2} u(\boldsymbol{\xi}), \partial_{x_3} u(\boldsymbol{\xi}), u(\boldsymbol{\xi})]$ at one quadrature point $\boldsymbol{\xi}$ into a single SIMD register.

Besides sum factorization, matrix-free operator evaluation involves computations at each quadrature point in steps (2), (5) and (9) of algorithm 1 which need to be vectorized as well. As the computations at different quadrature points are independent we process k quadrature points in parallel using SIMD instructions. This requires an additional in-place transpose operation illustrated here for $k = 4$:

$$\begin{bmatrix} \partial_{x_1} u(\boldsymbol{\xi}_l), & \partial_{x_2} u(\boldsymbol{\xi}_l), & \partial_{x_3} u(\boldsymbol{\xi}_l), & u(\boldsymbol{\xi}_l) \\ \partial_{x_1} u(\boldsymbol{\xi}_{l+1}), & \partial_{x_2} u(\boldsymbol{\xi}_{l+1}), & \partial_{x_3} u(\boldsymbol{\xi}_{l+1}), & u(\boldsymbol{\xi}_{l+1}) \\ \partial_{x_1} u(\boldsymbol{\xi}_{l+2}), & \partial_{x_2} u(\boldsymbol{\xi}_{l+2}), & \partial_{x_3} u(\boldsymbol{\xi}_{l+2}), & u(\boldsymbol{\xi}_{l+2}) \\ \partial_{x_1} u(\boldsymbol{\xi}_{l+3}), & \partial_{x_2} u(\boldsymbol{\xi}_{l+3}), & \partial_{x_3} u(\boldsymbol{\xi}_{l+3}), & u(\boldsymbol{\xi}_{l+3}) \end{bmatrix}$$

↓

$$\begin{bmatrix} \partial_{x_1} u(\boldsymbol{\xi}_l), & \partial_{x_1} u(\boldsymbol{\xi}_{l+1}), & \partial_{x_1} u(\boldsymbol{\xi}_{l+2}), & \partial_{x_1} u(\boldsymbol{\xi}_{l+3}) \\ \partial_{x_2} u(\boldsymbol{\xi}_l), & \partial_{x_2} u(\boldsymbol{\xi}_{l+1}), & \partial_{x_2} u(\boldsymbol{\xi}_{l+2}), & \partial_{x_2} u(\boldsymbol{\xi}_{l+3}) \\ \partial_{x_3} u(\boldsymbol{\xi}_l), & \partial_{x_3} u(\boldsymbol{\xi}_{l+1}), & \partial_{x_3} u(\boldsymbol{\xi}_{l+2}), & \partial_{x_3} u(\boldsymbol{\xi}_{l+3}) \\ u(\boldsymbol{\xi}_l), & u(\boldsymbol{\xi}_{l+1}), & u(\boldsymbol{\xi}_{l+2}), & u(\boldsymbol{\xi}_{l+3}) \end{bmatrix}$$

A second transpose operation is necessary after the quadrature point computations to achieve the correct layout for the subsequent sum factorization step. While the transpose steps add an additional overhead, this overhead is very small and can mostly be hidden behind the actual computations by loop unrolling. The remaining overhead is outweighed by the performance advantage in the sum factorization steps.

Our implementation precomputes and caches the local coordinates and associated weights of all quadrature points. These are then streamed from memory during steps (2), (5) and (9) of Algorithm 1, which allows us to use a flat iteration space during those steps. In our experience, the advantage of not having to use nested iteration or reconstruct the multi index i from a flat index by far outweighs the increased L1 cache pressure of having to load an additional $d + 1$ values per quadrature point.

p	Matrix-free A		Matrix-free B		Matrix-based		Matrix Assembly	
	$\frac{\text{DOF}}{s}$	$\frac{\text{GFLOP}}{s}$	$\frac{\text{DOF}}{s}$	$\frac{\text{GFLOP}}{s}$	$\frac{\text{DOF}}{s}$	$\frac{\text{GFLOP}}{s}$	$\frac{\text{DOF}}{s}$	$\frac{\text{GFLOP}}{s}$
1	1.70×10^8	104	1.19×10^8	321	2.06×10^8	24.3	1.60×10^7	345
2	3.93×10^8	238	2.52×10^8	450	6.42×10^7	27.3	8.71×10^6	371
3	5.38×10^8	328	3.30×10^8	524	2.69×10^7	29.8	4.66×10^6	368
4	5.95×10^8	387	3.88×10^8	560	9.54×10^6	23.5	2.57×10^6	301
5	6.17×10^8	424	4.03×10^8	568	4.58×10^6	23.3	1.93×10^6	307
6	5.99×10^8	439	4.06×10^8	563	2.31×10^6	23.5	1.21×10^6	231
7	5.70×10^8	442	3.98×10^8	556	1.46×10^6	30.3	6.65×10^5	143
8	5.41×10^8	445	3.85×10^8	541	6.14×10^5	24.1	8.74×10^5	198
9	5.05×10^8	439	3.70×10^8	530	2.98×10^5	26.2	7.01×10^5	133
10	4.71×10^8	432	3.59×10^8	524	—	—	—	—

TABLE 1

Full operator application, 2x Intel Xeon E5-2698v3 2.3 GHz, all 32 cores busy for two problems of different complexity and for comparison matrix assembly for the simpler problem and matrix-based operator application. Note that the matrix-based computations use significantly smaller problem sizes due to memory constraints.

We have implemented separate code paths for axis-parallel, affine and multilinear geometries. In the case of multilinear geometries the transformation $x = \mu_T(\hat{x})$ from the reference element \hat{T} to the real element T is a d -valued Q_1 finite element function and sum-factorization can be used to evaluate its values and derivatives at quadrature points. The same approach could also be used for higher order geometries.

The evaluation of face integrals poses an additional challenge: As outlined in Section 3.5, it is important to start (respectively end) with the face normal direction q_F^\pm in steps (4), (8) (respectively steps (6) and (10)) of algorithm 1 to obtain optimal computational complexity for sum factorization in face integrals. This does, however, complicate the memory access patterns in the first (respectively last) step of the sum factorization kernel, which causes a substantial performance reduction which is further exacerbated by the reduced size of the involved matrix (compared to volume integrals). In order to minimize this performance impact, we use C++ metaprogramming to generate dedicated versions of the face sum factorization kernels for all combinations of face normal directions.

Like other general-purpose finite element discretization frameworks, PDELab by default uses a temporary buffer to gather all degrees of freedom associated with a single element contiguously into memory before processing the element. Likewise, the computational results associated with one element are stored in a buffer and then scattered to corresponding locations in the global data structure. These gather and scatter operations are, however, not necessary in discontinuous Galerkin methods where the global data may already be arranged contiguously in memory. We thus extended PDELab with a DG-specific code path that exploits the block structure of DG problems avoiding any superfluous copy operations.

5. Numerical Results. In order to measure the efficiency of our numerical approach and implementation, we are most importantly interested in the time to solution for a given accuracy. As the aim of this paper is high-performance operator application, we are right now merely interested in the time required for this operation. In order to keep operator applications comparable across different polynomial degrees with different problem sizes and matrix-free / matrix-based approaches, we measure the number of DOFs/s that we can process during the operator application.

Moreover, as the operator application itself is a completely local operation and does not require communication, we begin by studying its behavior on a single node compute node. For all of the following measurements, we used a node of our workgroup cluster that is equipped with 2x Intel Xeon E5-2698v3 2.3 GHz Haswell processors (16 cores and 40 MiB of L3 cache each) and 128 GiB of DDR3-2133 RAM with deactivated Hyperthreading and deactivated Turbo Mode. The peak floating point performance of this processor can only be attained using fused multiply-add instructions; at the maximum throughput rate of 2 FMA instructions/cycle, this processor is capable of a theoretical peak of 486.4 GFLOPs (while the vector math units are active, the processor speed is reduced to 1.9 GHz for thermal management), yielding a total of 972.8 GFLOPs / node. In order to achieve this performance, the calculations must expose a considerable amount of independent operations, as the FMA instructions on this processor have a latency of 5 clock cycles and we thus need to expose $2 \cdot 5 \cdot 4 = 40$ independent FMA chains. Moreover, as the processor relies on SIMD registers of width 4, the operations must be grouped into blocks of that size operating on adjacent memory locations as this processor does not support strided loads and stores with good performance. This problem is further exacerbated by the limited number of available processor registers (16), which requires us to reuse registers when feeding data to the FMA units of the processor, as each of the 10 vector operations in flight at peak performance requires 3 registers (two input registers and one input / output register).

In order to avoid spurious performance effects due to under-utilized resources, we run our benchmarks as MPI-parallel programs with 32 ranks, one pinned to each core of the node. The meshes for problems of different polynomial degree are sized in such a way that the number of DOFs is approximately constant ($\approx 4 \cdot 10^8$), resulting in input and output vectors of about 3.2 GiB each in total to avoid any possible cache effects.

5.1. Model Problems. As we want to model the performance as part of a much larger computation involving additional nodes, we set up a test problem with periodic boundary conditions in all directions. PDELab implements periodic boundaries in the same way as regular processor boundaries, which results in an ideally load-balanced computation.

We test our implementation with three different problems of increasing computational intensity. All problems are convection-diffusion-reaction problems with tensor-valued diffusion coefficients and use weighted averaging across cell boundaries for discontinuous coefficients:

Problem A has axis-parallel cells and coefficients that are constant per cell. It is a baseline model that we expect to perform best in terms of throughput (DOFs/sec), but not necessarily in efficiency (GFLOPs/sec), due to the low amount of work per DOF.

Problem B is an intermediate problem with affine geometries and coefficients that are polynomials in the coordinates.

Problem C is a computationally intensive problem with multilinear geometries and coefficients that are polynomials in the coordinates.

A central question related to these problems is the required integration order q : For Problem A, we can choose $q = 2p$ (which yields $n = m = p + 1$ as in the theoretical discussion in 3.6). As the diffusion tensor in Problem B/C is a polynomial in \mathbf{x} , we increase q to $q = 2p + 4$. Problem C models a situation where most/all geometries are nonlinear and as such, the inverse determinant of the geometry Jacobian becomes a

rational function in \mathbf{x} . In contrast to first-order PDEs, where this term cancels out, it is very much present in our second-order example. In order to minimize the quadrature error, we have (somewhat arbitrarily) picked $q = 3p + 4$ for the final problem. Note that in actual applications, non-linear geometries can often be restricted to small parts of the mesh. By contrast, we have chosen Problem C to highlight the performance impact of more complex geometries and/or coefficients.

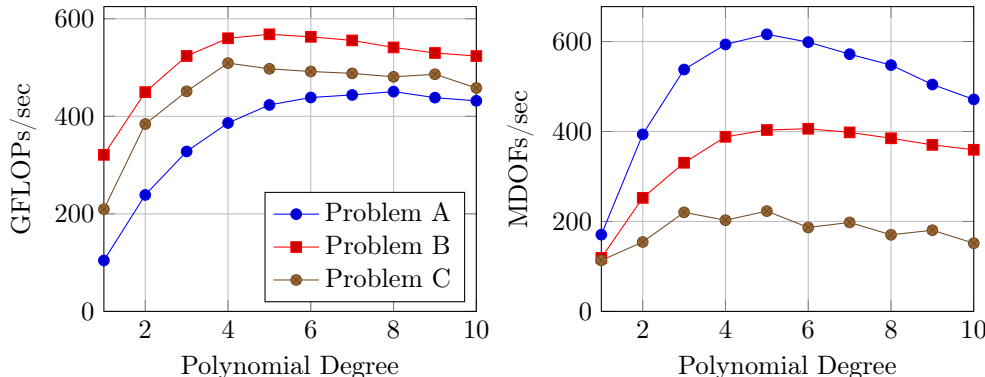


FIG. 4. Floating point performance in GFLOPs/sec and throughput in MDOFs/sec for full operator application, 2x Intel Xeon E5-2698v3 2.3 GHz for all model problems

5.2. Comparison To Matrix-Based Operator Application. Table 1 shows the throughput and the hardware efficiency of our matrix-free code for Problem A and Problem B. For comparison, we also assemble the matrix of the operator (again using our sum-factorized implementation) and apply the resulting matrix to an input vector using matrix-vector multiplication. Those results are also shown in Table 1; they were obtained using PETSc [2, 3] using block compressed row format to exploit the block structure of DG. Note that the problems had to be scaled down a lot for the matrix-based computations in order to fit the matrix into memory: For $p = 3$, the matrix-based problem is about 15 times smaller, while for $p = 9$, the factor is ≈ 1300 . Our matrix-free implementation outperforms the matrix-vector product for $p > 1$ or $p > 2$ (simple/expensive problem). However, even at low degrees the performance advantage of the matrix-based version is somewhat reduced by the fact that assembling the matrix also takes a significant amount of time in addition to severely reducing the number of DOFs that can fit into a given amount of RAM.

Figure 4 compares throughput and floating point performance of our implementation for the three problems described above. With increasing complexity (i.e., more work per DOF), throughput decreases by a factor of ≈ 3 when going from Problem A to Problem C. On the other hand, the higher computational intensity affords better as demonstrated by the the GFLOPs/sec rates, which reach up to about 60% peak for Problem B. Problem C’s performance falls between that of the other two problems; while it provides the most work/DOF, the additional sum factorization operations for the coordinates are only polynomials with $p_C = 1$, and with increasing p we start to exhaust the L1 cache due to the large number of quadrature points.

5.3. Intra-Node Scalability. Next, we look at the weak scalability of matrix-free and matrix-based operator application on a single compute node, which provides

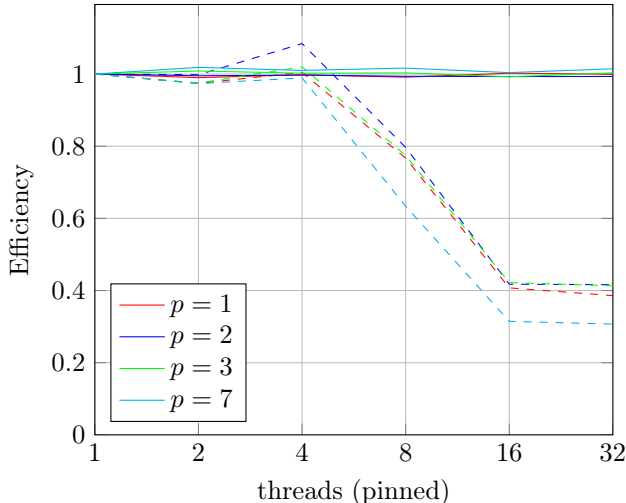


FIG. 5. Weak scaling of operator application on single node. Processes pinned to individual cores, runs with 1-16 processes pinned to a single socket and 32 processes across two sockets. Solid lines denote matrix-free computations, dashed lines matrix-based.

insight into the load placed on parts of the processor shared across multiple cores (memory interfaces, I/O, etc.). As shown in Figure 5, our matrix-free operator application scales perfectly to all cores of the machine, while the matrix-based version breaks down beyond 4 cores per socket. This behavior can be explained by the roofline model (cf. Figure 2): The matrix-based implementation is memory-bound, and as the processor in our machine is equipped with 4 memory controllers, their bandwidth has to be shared across multiple cores. The matrix-free code is compute-bound and thus not restricted by resources shared between multiple cores. The cores are pinned to sockets in such a way that we first saturate one socket before allocating cores on the second socket. Thus the step from 16 to 32 cores is balanced in the matrix-based case by the additional 4 memory controllers on the second socket.

5.4. Realistic Example Problem. In addition to measuring the performance of our code in isolation, we also apply it to a more complete problem setting. We study the full instationary transport problem (1) with highly convection-dominated flow on a periodic domain $\Omega = (-\pi, \pi)^3$ with $D = 5 \cdot 10^{-6} \cdot \mathbb{I}$, $c = 0$, $f = 0$ and a fixed flow field of Taylor-Green type [46]:

$$(22) \quad \mathbf{b}(\mathbf{x}) = \begin{pmatrix} \cos(x_1) \sin(-x_2) \sin(-x_3) \\ \frac{1}{2} \sin(x_1) \cos(-x_2) \sin(-x_3) \\ \frac{1}{2} \sin(x_1) \sin(-x_2) \cos(-x_3) \end{pmatrix}.$$

We then compute the evolution of an initial concentration u_0 given by a Gaussian centered around $x_0 = (\frac{1}{2}, 0, 0)$ as $u_0 = \exp(-2\|x - x_0\|^2)$.

This problem is computationally quite expensive due to the trigonometric function evaluations at each quadrature point and the increased quadrature order required for those functions (we have chosen $q = 2 * p + 4$ here). The trigonometric functions are evaluated using optimized and vectorized implementations from [27].

In order to limit the scope of this discussion, we use a strong stability preserving second-order explicit time stepping scheme (Heun). In combination with the DG discretization, this yields a block-diagonal mass matrix, and by choosing Legendre basis

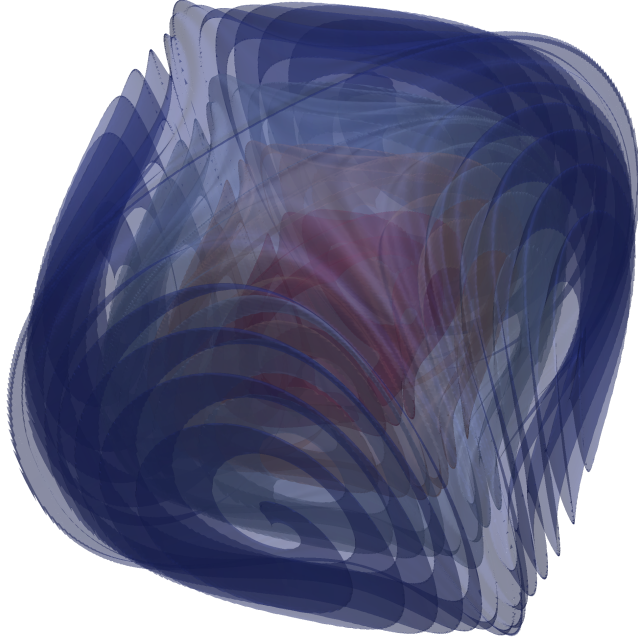


FIG. 6. Isocontours for $u \in \{0.13, 0.25, 0.38, 0.51, 0.64\}$ at $t = 140$ for the Taylor-Green example problem with polynomial degree 5 and mesh size 240^3 ($\approx 3 \cdot 10^9$ DOFs, 165000 time steps, 143000 core hours on 6144 cores including I/O).

functions, we even obtain a point-diagonal mass matrix, eliminating any occurrences of non-trivial linear equation systems in our solver. We calculate the inverse mass matrix in a setup step, and as a result, our solver only performs matrix-free residual calculations and products of a diagonal matrix with a vector, combined with halo exchanges to keep the solution consistent across subdomains.

The periodic boundary conditions of the problem ensure that all subdomains of the problem are identically structured, which guarantees ideal load balancing.

Figure 6 shows the concentration at $t = 140$ for a simulation with 240^3 cells and polynomial degree $p = 5$. As can be seen in the image, the prescribed flow field creates a very complex structure that requires a very high resolution to capture the solution well.

5.5. Scalability Studies for Realistic Example Problem. As we are ultimately interested in HPC, we investigate the scalability of our implementation on the moderately sized *bufordev* development cluster in Heidelberg, which consists of 416 compute nodes with 2 x E5-2630 v3 processors each (Haswell architecture with 16 cores / node, 64 GiB / node) and uses a QDR Infiniband interconnect with a fully connected two-level topology. Figure 7 shows the efficiency of weakly scaling our realistic example problem 5.4 for $p = 3$ with $\approx 10^6$ DOFs / core from 1 to 384 nodes of the cluster.

Our solver is only made up of local computations and halo exchanges, so we expect the mostly flat efficiency curve observed in our measurements; the slight performance degradation at larger problem sizes is mostly due to the increased communication jitter as the program starts to span more of the cluster's communication infrastructure.

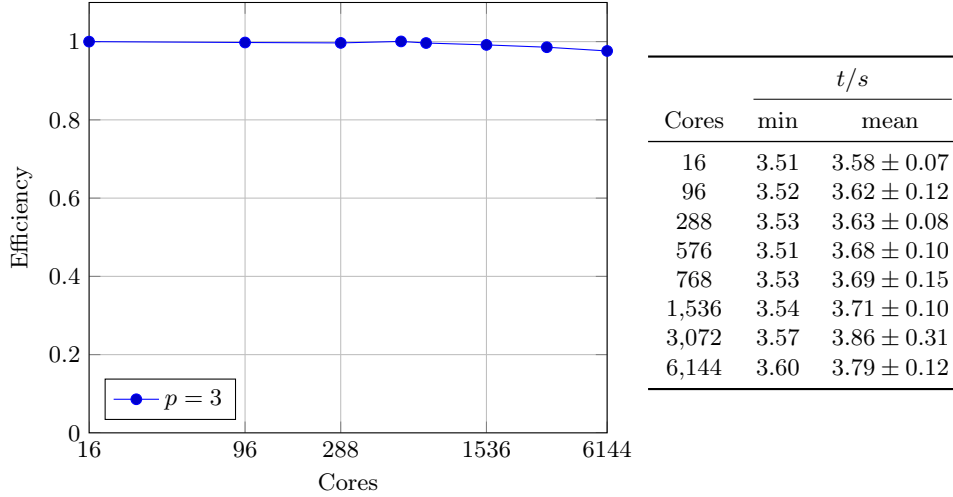


FIG. 7. Efficiency and run times for weak scalability on IWR compute cluster (416 nodes with 2 x E5-2630 v3 each, 64 GiB / node, QDR Infiniband). The plot is based on the fastest times, mean values show a large amount of timing jitter as seen in the table.

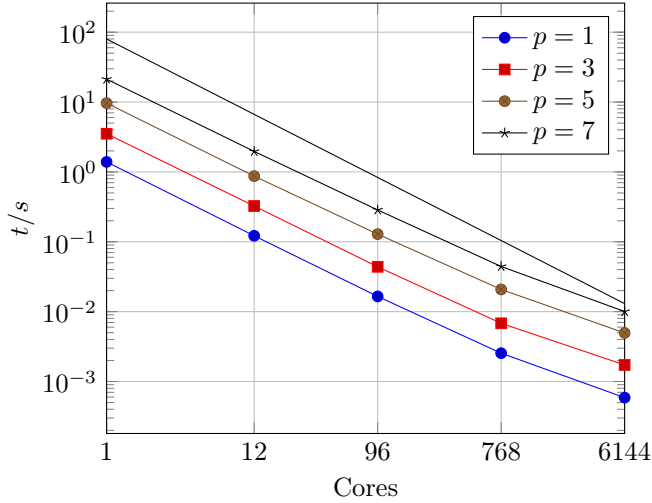


FIG. 8. Run times for strong scalability on IWR compute cluster (416 nodes with 2 x E5-2630 v3 each, 64 GiB / node, QDR Infiniband)

The results of our strong scalability benchmarks are shown in Figure 8. Due to the low memory footprint of our matrix-free solver, we are able to measure scalability from 1 to 6144 cores on up to 384 nodes. Across this range, the mesh size per core shrinks from 48^3 to $3 \times 3 \times 2$ cells, which corresponds to between 10^2 and 10^5 DOFs per core at 6144 cores, depending on p . For these very small working sets, scalability suffers mostly because our implementation is currently not able to overlap computation and halo communication, which can be seen in more detail in Table 2.

6. Conclusion. We have presented an efficient implementation of a high-order Discontinuous Galerkin discretization for convection-diffusion-reaction problems that

Cores	Q_1		Q_3		Q_5		Q_7	
	t/s	η	t/s	η	t/s	η	t/s	η
1	1.39	1.00	3.52	1.00	9.65	1.00	2.12×10^1	1.00
12	1.22×10^{-1}	0.95	3.25×10^{-1}	0.90	8.71×10^{-1}	0.92	1.97	0.90
96	1.65×10^{-2}	0.88	4.38×10^{-2}	0.84	1.29×10^{-1}	0.78	2.85×10^{-1}	0.78
768	2.54×10^{-3}	0.71	6.81×10^{-3}	0.67	2.08×10^{-2}	0.60	4.43×10^{-2}	0.62
6,144	5.88×10^{-4}	0.39	1.73×10^{-3}	0.33	4.95×10^{-3}	0.32	1.00×10^{-2}	0.34

TABLE 2

Run times and efficiencies η for strong scalability on IWR compute cluster (416 nodes with 2 x E5-2630 v3 each, 64 GiB / node, QDR Infiniband)

uses sum factorization for optimal algorithmic complexity. Our implementation exploits the inherent structure of this numerical scheme and delivers more than 50% of the theoretical peak performance on AVX2-based Intel architectures with fused multiply-add operations, which make up the majority of compute power in current large-scale compute clusters that is not backed by accelerators. At the same time, our implementation does not require vectorization over multiple cells or faces and can thus be integrated into existing frameworks without having to restructure framework code.

For clarity, we have focused in this paper on operator application for scalar problems. In a separate paper, we apply the presented techniques to a Navier-Stokes solver[40], while an upcoming paper will investigate efficient preconditioners within this framework without sacrificing the performance and memory advantages of our approach. At the same time, developing this type of highly optimized code in C++ is very time consuming and highly affected by the type of problem under investigation and by hardware developments. For this reason, we are also working on a Python-based code generation tool that can transform a very abstract description of the weak form into highly optimized code. This tool can already handle complex systems of equations and generate code using the AVX-512 instruction set for newer versions of Xeon processors as well as the Xeon Phi accelerator architecture. We will describe it in detail in another upcoming paper.

REFERENCES

- [1] K. ASANOVIC, R. BODIK, J. DEMMEL, T. KEAVENY, K. KEUTZER, J. KUBIATOWICZ, N. MORGAN, D. PATTERSON, K. SEN, J. WAWRZYNEK, D. WESSEL, AND K. YELICK, *A view of the parallel computing landscape*, Commun. ACM, 52 (2009), pp. 56–67, <https://doi.org/10.1145/1562764.1562783>, <http://doi.acm.org/10.1145/1562764.1562783>.
- [2] S. BALAY, S. ABHYANKAR, M. F. ADAMS, J. BROWN, P. BRUNE, K. BUSCHELMAN, L. DALCIN, V. EIJKHOUT, W. D. GROPP, D. KAUSHIK, M. G. KNEPLEY, D. A. MAY, L. C. MCINNES, K. RUPP, P. SANAN, B. F. SMITH, S. ZAMPINI, H. ZHANG, AND H. ZHANG, *PETSc users manual*, Tech. Report ANL-95/11 - Revision 3.8, Argonne National Laboratory, 2017, <http://www.mcs.anl.gov/petsc>.
- [3] S. BALAY, S. ABHYANKAR, M. F. ADAMS, J. BROWN, P. BRUNE, K. BUSCHELMAN, L. DALCIN, V. EIJKHOUT, W. D. GROPP, D. KAUSHIK, M. G. KNEPLEY, D. A. MAY, L. C. MCINNES, K. RUPP, B. F. SMITH, S. ZAMPINI, H. ZHANG, AND H. ZHANG, *PETSc Web page*. <http://www.mcs.anl.gov/petsc>, 2017, <http://www.mcs.anl.gov/petsc>.
- [4] P. BASTIAN, *Benchmark 3d: Symmetric weighted interior penalty discontinuous galerkin scheme*, in Finite Volumes for Complex Applications VI Problems & Perspectives, J. Fürst, J. Halama, R. Herbin, and F. Hubert, eds., vol. 4 of Springer Proceedings in Mathematics, Springer Berlin Heidelberg, 2011, pp. 949–959, <https://doi.org/10.1007/>

- 978-3-642-20671-9_92, http://dx.doi.org/10.1007/978-3-642-20671-9_92.
- [5] P. BASTIAN, *A fully-coupled discontinuous galerkin method for two-phase flow in porous media with discontinuous capillary pressure*, Computational Geosciences, 18 (2014), pp. 779–796, <https://doi.org/10.1007/s10596-014-9426-y>, <http://dx.doi.org/10.1007/s10596-014-9426-y>.
 - [6] P. BASTIAN, M. BLATT, A. DEDNER, C. ENGWER, R. KLÖFKORN, R. KORNHUBER, M. OHLBERGER, AND O. SANDER, *A generic grid interface for parallel and adaptive scientific computing. part II: implementation and tests in DUNE*, Computing, 82 (2008), pp. 121–138, <https://doi.org/10.1007/s00607-008-0003-x>.
 - [7] P. BASTIAN, M. BLATT, A. DEDNER, C. ENGWER, R. KLÖFKORN, M. OHLBERGER, AND O. SANDER, *A generic grid interface for parallel and adaptive scientific computing. part I: abstract framework*, Computing, 82 (2008), pp. 103–119, <https://doi.org/10.1007/s00607-008-0003-x>.
 - [8] P. BASTIAN, M. BLATT, AND R. SCHEICHL, *Algebraic multigrid for discontinuous Galerkin discretizations*, Numer. Linear Algebra Appl., 19 (2012), pp. 367–388, <https://doi.org/10.1002/nla.1816>.
 - [9] P. BASTIAN, C. ENGWER, J. FAHLKE, M. GEVELER, D. GGÖDDEKE, O. ILIEV, O. IPI-SCH, R. MILK, J. MOHRING, S. MÜTHING, M. OHLBERGER, D. RIBBROCK, AND S. TUREK, *Hardware-based efficiency advances in the exa-dune project*, in Software for Exascale Computing - SPPEXA 2013-2015, vol. 113 of LNCSE, Springer-Verlag, 2016, <https://doi.org/10.1007/978-3-319-40528-5>.
 - [10] P. BASTIAN, F. HEIMANN, AND S. MARNACH, *Generic implementation of finite element methods in the distributed and unified numerics environment (DUNE)*, Kybernetika, 46 (2010), pp. 294–315.
 - [11] P. BASTIAN AND B. RIVIÈRE, *Superconvergence and $H(\text{div})$ -projection for discontinuous Galerkin methods*, Int. J. Numer. Meth. Fluids., 42 (2003), pp. 1043–1057, <https://doi.org/10.1002/flid.562>.
 - [12] P. E. BUIS AND W. R. DYKSEN, *Efficient vector and parallel manipulation of tensor products*, ACM Trans. Math. Softw., 22 (1996), pp. 18–23, <https://doi.org/10.1145/225545.225548>, <http://doi.acm.org/10.1145/225545.225548>.
 - [13] B. COCKBURN, J. GOPALAKRISHNAN, AND R. LAZAROV, *Unified hybridization of discontinuous galerkin, mixed, and continuous galerkin methods for second order elliptic problems*, SIAM Journal on Numerical Analysis, 47 (2009), pp. 1319–1365, <https://doi.org/10.1137/070706616>.
 - [14] B. COCKBURN, S. LIN, AND C. SHU, eds., *Discontinuous Galerkin methods. Theory, computation and applications*, vol. 11 of Lecture Notes in Computational Science and Engineering, Springer-Verlag, 2000.
 - [15] K. DATTA, M. MURPHY, V. VOLKOV, S. WILLIAMS, J. CARTER, L. OLIKER, D. PATTERSON, J. SHALF, AND K. YELICK, *Stencil computation optimization and auto-tuning on state-of-the-art multicore architectures*, in Proceedings of the 2008 ACM/IEEE Conference on Supercomputing, SC '08, Piscataway, NJ, USA, 2008, IEEE Press, pp. 4:1–4:12, <http://dl.acm.org/citation.cfm?id=1413370.1413375>.
 - [16] D. DI PIETRO AND A. ERN, *Mathematical Aspects of Discontinuous Galerkin Methods*, Springer, 2012.
 - [17] D. DI PIETRO, A. ERN, AND J.-L. GUERMOND, *Discontinuous galerkin methods for anisotropic semidefinite diffusion with advection*, SIAM J. Numer. Anal., (2008).
 - [18] J. DONGARRA, *Report on the sunway taihulight system*, Tech. Report UT-EECS-16-742, Oak Ridge National Laboratory, 2016.
 - [19] J. DONGARRA, P. BECKMAN, T. MOORE, P. AERTS, G. ALOISIO, J.-C. ANDRE, D. BARKAI, J.-Y. BERTHOU, T. BOKU, B. BRAUNSCHWEIG, F. CAPPELLO, B. CHAPMAN, C. XUEBIN, A. CHOUDHARY, S. DOSANJH, T. DUNNING, S. FIORE, A. GEIST, B. GROPP, R. HARRISON, M. HERELD, M. HEROUX, A. HOISIE, K. HOTTA, J. ZHONG, Y. ISHIKAWA, F. JOHNSON, S. KALE, R. KENWAY, D. KEYES, B. KRAMER, J. LABARTA, A. LICHNEWSKY, T. LIPPERT, B. LUCAS, B. MACCABE, S. MATSUOKA, P. MESSINA, P. MICHIELSE, B. MOHR, M. MUELLER, W. NAGEL, H. NAKASHIMA, M. E. PAPKA, D. REED, M. SATO, E. SEIDEL, J. SHALF, D. SKINNER, M. SNIR, T. STERLING, R. STEVENS, F. STREITZ, B. SUGAR, S. SUMIMOTO, W. TANG, J. TAYLOR, R. THAKUR, A. TREFETHEN, M. VALERO, A. VAN DER STEEN, J. VETTER, P. WILLIAMS, R. WISNIEWSKI, AND K. YELICK, *The international exascale software project roadmap*, International Journal of High Performance Computing Applications, 25 (2011), pp. 3–60, <https://doi.org/10.1177/1094342010391989>.
 - [20] J. DONGARRA, J. HITTERGER, J. BELL, L. CHACÓN, R. FALGOUT, M. HEROUX, P. HOVLAND,

- E. NG, C. WEBSTER, S. WILD, AND K. PAO, *Applied mathematics research for exascale computing*, tech. report, U.S. Department of Energy, Office of Science, Advanced Scientific Computing Research Program, 2014. <http://science.energy.gov/media/ascr/pdf/research/am/docs/EMWGreport.pdf>.
- [21] C. C. DOUGLAS, J. HU, W. KARL, M. KOWARSCHIK, U. RÜDE, AND C. WEISS, *Fixed and Adaptive Cache Aware Algorithms for Multigrid Methods*, Springer Berlin Heidelberg, Berlin, Heidelberg, 2000, pp. 87–93, https://doi.org/10.1007/978-3-642-58312-4_11, http://dx.doi.org/10.1007/978-3-642-58312-4_11.
- [22] H. ELMAN, D. SILVESTER, AND A. WATHEN, *Finite Elements and Fast Iterative Solvers*, Oxford University Press, 2005.
- [23] A. ERN AND J. GUERMOND, *Theory and practice of finite element methods*, Springer, 2004.
- [24] A. ERN, I. MOZOLEVSKI, AND L. SCHUH, *Discontinuous galerkin approximation of two-phase flows in heterogeneous porous media with discontinuous capillary pressures*, *Computer Methods in Applied Mechanics and Engineering*, 199 (2010), pp. 1491 – 1501, <https://doi.org/10.1016/j.cma.2009.12.014>.
- [25] A. ERN, S. NICAISE, AND M. VOHRALÍK, *An accurate $H(\text{div})$ flux reconstruction for discontinuous galerkin approximations of elliptic problems*, *C. R. Math. Acad. Sci. Paris*, 345 (2007), pp. 709–712.
- [26] A. ERN, A. F. STEPHANSEN, AND P. ZUNINO, *A discontinuous Galerkin method with weighted averages for advection-diffusion equations with locally small and anisotropic diffusivity*, *IMA Journal of Numerical Analysis*, 29 (2009), pp. 235–256, <https://doi.org/10.1093/imanum/drm050>.
- [27] A. FOG, *VCL C++ vector class library*, 2017, <http://www.agner.org/optimize/vectorclass.pdf>.
- [28] B. GMEINER, U. RÜDE, H. STENGEL, C. WALUGA, AND B. WOHLMUTH, *Performance and scalability of hierarchical hybrid multigrid solvers for Stokes systems*, *SIAM Journal on Scientific Computing*, 37 (2015), pp. C143–C168, <https://doi.org/10.1137/130941353>.
- [29] A. HEINECKE, G. HENRY, M. HUTCHINSON, AND H. PABST, *Libxsmm: Accelerating small matrix multiplications by runtime code generation*, in *SC16: International Conference for High Performance Computing, Networking, Storage and Analysis (SC)*, IEEE Computer Society, 2016, pp. 981–991, <https://doi.org/10.1109/SC.2016.83>.
- [30] H. HUANG AND G. SCOVAZZI, *A high-order, fully coupled, upwind, compact discontinuous galerkin method for modeling of viscous fingering in compressible porous media*, *Computer Methods in Applied Mechanics and Engineering*, 263 (2013), pp. 169 – 187, <https://doi.org/http://dx.doi.org/10.1016/j.cma.2013.04.010>, <http://www.sciencedirect.com/science/article/pii/S0045782513001084>.
- [31] G. KARNIADAKIS AND S. SHERWIN, *Spectral/hp Element Methods for CFD*, Oxford University Press, 2005.
- [32] D. E. KEYES, *Exaflop/s: The why and the how*, *Comptes Rendus Mécanique*, 339 (2011), pp. 70–77, <https://doi.org/10.1016/j.crme.2010.11.002>.
- [33] M. KREUTZER, G. HAGER, G. WELLEIN, H. FEHSKE, AND A. R. BISHOP, *A unified sparse matrix data format for efficient general sparse matrix-vector multiplication on modern processors with wide simd units*, *SIAM Journal on Scientific Computing*, 36 (2014), pp. C401–C423, <https://doi.org/10.1137/130930352>.
- [34] M. KRONBICHLER AND K. KORMANN, *A generic interface for parallel cell-based finite element operator application*, *Computers & Fluids*, 63 (2012), pp. 135–147, <https://doi.org/10.1016/j.compfluid.2012.04.012>.
- [35] J. LI AND B. RIVIERE, *Numerical solutions of the incompressible miscible displacement equations in heterogeneous media*, *Computer Methods in Applied Mechanics and Engineering*, 292 (2015), pp. 107 – 121, <https://doi.org/http://dx.doi.org/10.1016/j.cma.2014.10.048>, <http://www.sciencedirect.com/science/article/pii/S0045782514004186>. Special Issue on Advances in Simulations of Subsurface Flow and Transport (Honoring Professor Mary F. Wheeler).
- [36] X. LIU, M. SMELYANSKIY, E. CHOW, AND P. DUBEY, *Efficient sparse matrix-vector multiplication on x86-based many-core processors*, in *Proceedings of the 27th International ACM Conference on International Conference on Supercomputing, ICS '13, New York, NY, USA, 2013*, ACM, pp. 273–282, <https://doi.org/10.1145/2464996.2465013>, <http://doi.acm.org/10.1145/2464996.2465013>.
- [37] J. MELENK, K. GERDES, AND C. SCHWAB, *Fully discrete hp-finite elements: fast quadrature*, *Computer Methods in Applied Mechanics and Engineering*, 190 (2001), pp. 4339–4364, [https://doi.org/10.1016/S0045-7825\(00\)00322-4](https://doi.org/10.1016/S0045-7825(00)00322-4).
- [38] A. NGO, P. BASTIAN, AND O. IPPISCH, *Numerical solution of steady-state groundwater flow and solute transport problems: Discontinuous galerkin based methods compared to the*

- streamline diffusion approach*, Computer Methods in Applied Mechanics and Engineering, 294 (2015), pp. 331 – 358, <https://doi.org/http://dx.doi.org/10.1016/j.cma.2015.06.008>, <http://www.sciencedirect.com/science/article/pii/S0045782515002005>.
- [39] S. A. ORSZAG, *Spectral methods for problems in complex geometries*, Journal of Computational Physics, 37 (1980), pp. 70 – 92, [https://doi.org/http://dx.doi.org/10.1016/0021-9991\(80\)90005-4](https://doi.org/http://dx.doi.org/10.1016/0021-9991(80)90005-4), <http://www.sciencedirect.com/science/article/pii/0021999180900054>.
- [40] M. PIATKOWSKI, S. MÜTHING, AND P. BASTIAN, *A stable and high-order accurate discontinuous galerkin based splitting method for the incompressible navier-stokes equations*, J. Comput. Physics, accepted (2017), <https://arxiv.org/abs/1612.00657>.
- [41] D. A. D. PIETRO AND A. ERN, *Hybrid high-order methods for variable-diffusion problems on general meshes*, Comptes Rendus Mathematique, 353 (2015), pp. 31 – 34, <https://doi.org/https://doi.org/10.1016/j.crma.2014.10.013>, <http://www.sciencedirect.com/science/article/pii/S1631073X1400257X>.
- [42] J. RUDI, A. C. I. MALOSI, T. ISAAC, G. STADLER, M. GURNIS, P. W. J. STAAR, Y. INEICHEN, C. BEKAS, A. CURIONI, AND O. GHATTAS, *An extreme-scale implicit solver for complex pdes: Highly heterogeneous flow in earth’s mantle*, in Proceedings of the International Conference for High Performance Computing, Networking, Storage and Analysis, SC ’15, New York, NY, USA, 2015, ACM, pp. 5:1–5:12, <https://doi.org/10.1145/2807591.2807675>, <http://doi.acm.org/10.1145/2807591.2807675>.
- [43] J. SCHÖBERL, *C++11 implementation of finite elements in ngsolve*, Tech. Report 30, Institute for Analysis and Scientific Computing – Vienna University of Technology, 2014.
- [44] S. SELLAPPA AND S. CHATTERJEE, *Cache-efficient multigrid algorithms*, Int. J. High Perform. Comput. Appl., 18 (2004), pp. 115–133, <https://doi.org/10.1177/1094342004041295>, <http://dx.doi.org/10.1177/1094342004041295>.
- [45] C. SHU, *Total-variation-diminishing time discretizations*, SIAM J. Sci. Stat. Comput., 9 (1988), p. 1073.
- [46] G. I. TAYLOR AND A. E. GREEN, *Mechanism of the production of small eddies from large ones*, Proceedings of the Royal Society of London. Series A, Mathematical and Physical Sciences, 158 (1937), pp. 499–521, <http://www.jstor.org/stable/96892>.
- [47] M. V. WILKES, *The memory gap and the future of high performance memories*, SIGARCH Comput. Archit. News, 29 (2001), pp. 2–7, <https://doi.org/10.1145/373574.373576>, <http://doi.acm.org/10.1145/373574.373576>.